Multibody System Dynamics **11:** 209–233, 2004.

A Regularized Contact Model with Asymmetric Damping and Dwell-Time Dependent Friction

YVES GONTHIER[1], JOHN MCPHEE[2], CHRISTIAN LANGE[1] and JEAN-CLAUDE PIEDBŒUF[1]

[1] *Space Technologies, Canadian Space Agency, 6767 Route de l'Aéroport, St-Hubert, Québec, Canada, J3Y 8Y9; E-mail: yves.gonthier@space.gc.ca, christian.lange@space.gc.ca, jean-claude.piedboeuf@space.gc.ca*

[2] *Systems Design Engineering, University of Waterloo, Ontario, Canada N2L 3G1; E-mail: mcphee@real.uwaterloo.ca*

(Received: 31 July 2002; accepted in revised form: 18 December 2003)

Abstract. A general regularized contact model, including normal compliance, energy dissipation, and tangential friction, is described in this paper. The normal damping coefficient is formulated as a function of the coefficient of restitution e and the impact velocity only; the results are energy-consistent, with continuous force progression at the beginning and end of the impact, for both small and large values of e. The introduced seven parameter friction model based on an explicit formulation of the friction forces is suitable for real-time applications. The friction forces are split into its sliding and sticking contribution and a temporal lag effect, the dwell-time, is included using a novel dwell-time dependent stick state variable. Several examples are presented to demonstrate the features of this general contact model. The simulation results for a double pendulum hitting a plane are obtained, and a comparison with a benchmark problem shows the model behavior is in good agreement with published results.

Key words: contact dynamics, friction, coefficient of restitution.

1. Introduction

In the setting of the International Space Station Program, Canada is responsible for the verification of all tasks involving the Special Purpose Dextrous Manipulator (SPDM) [25]. In this context hardware-in-the-loop simulations (HLS) have been successfully applied for tasks involving contact dynamics [7]. However, the HLS concept turns out to be very costly and material-intensive. Alternatively, simulation can be used to complete the task verification. But this requires the development of accurate models for contact situations with friction, applicable for typical robotic tasks at low velocities.

The contact models must have minimal computational overhead since the entire simulation will be running on a real-time system operating at 1000 Hz. The time allowed to perform all the computations, including those required for the contact dynamics, must always remain below 1 ms. Most real-time simulation systems

utilize fixed-step explicit integrators such as Runge–Kutta or even Euler to maintain a predictable computation time. The contact models must therefore be compatible with these ODE solvers.

Traditionally, impact responses are predicted by rigid-body models in conjunction with impact hypotheses, such as Newton's, Poisson's, and Stronge's [8, 10, 29, 32]. Hereby, the equations of motion are derived by balancing the system's momenta before and after the impact, i.e., without explicitly considering contact compliances. This is also known as piecewise analysis [16].

For the direct central and frictionless impact, the coefficient of restitution e is used to express energy dissipation, relating, depending on the impact hypothesis, either velocities (Newton), impulses (Poisson), or energies (Stronge) before and after the impact as used in the works by e.g. Wittenburg [35], Wehage [33], and Lankarani and Nikravesh [17].

However, these rigid-body approaches neglect the small displacements occurring during collision. This allows for great simplifications since changes in velocity become instantaneous, and can be calculated without integrating accelerations over the contact period, but it leads to a loss of information about the contact forces that cause these changes in velocities. Also, in the case of the SPDM, the manipulator itself is flexible, and this results in impact durations in the order of 50 ms when the manipulated payloads come into contact with the environment. As a result, the impact duration cannot be assumed to be instantaneous.

In contrast, compliance models – also known as regularized models – describe the rate-dependent normal and tangential compliance relations over time. Furthermore, the stiffness properties can be directly related to the interfering geometries and, hence, a model more related to physical quantities can be derived.

Typical regularized models consist of a combination of spring and damper elements with linear or nonlinear force characteristics. For direct central and frictionless impacts Hunt and Crossley [11], Khulief and Shabana [15], and Lankarani and Nikravesh [17] use a continuous contact model with a local compliance in the normal direction. The energy dissipation is a function of a damping constant which can be related to the impact velocity and the coefficient of restitution. Marhefka and Orin [24] demonstrated the validity of the expression for the damping, and that the derived formulations are only valid for e close to unity.

If friction is also present, static and kinetic coefficients of friction, μ_S and μ_C, are applied additionally to relate normal and tangential forces during the sticking and sliding states, as shown in e.g. [3, 10, 14, 32, 34]. An extension of the above mentioned models can be found in [22] in which the impact of rigid bodies, including friction and energy dissipation, is modelled using a regularized approach with spring, dash-pot elements and hysteresis in normal and tangential directions.

Tenaglia et al. [30], Stronge [29] and Ma [23] also extended the direct central frictionless contact force model to three dimensions by adding a tangential compliance effect to model the friction. Friction models using local compliance are also known as bristle models [6]. However, the proposed models do not take into

account the dependency of the static friction on the time of contact, the so-called dwell-time [26].

This paper introduces a novel three-dimensional contact force model. The model can be used to simulate fully elastic to completely plastic impacts that are in direct central as well as eccentric configurations. The contact phase can be intermittent or lasting. In the latter case, the friction model will handle stationary as well as rolling contact situations. Frictional effects, such as stick-slip transition and static friction dwell-time dependency, are included in this model. It is shown how the proposed model can be implemented for any geometry where the contact area is small in comparison to the dimensions of the body. Simulation results for several examples are included.

2. A Regularized Contact Model

The term regularized describes the reformulation of a problem to derive a solvable formulation [20]. The contact forces are described as a function of the contact deformation by smoothening the discontinuity of the impact and friction forces in the constraints [5, 31]. Hertz's theory provides a good approximation of the contact force between hard compact bodies where the contact region remains small in comparison with the size of either body. Hence, the force approach law based on Hertzian theory is a regularization of the contact force problem.

For non-conforming elastic bodies, the local deformations in the contact region resulting from the reaction forces will create a small area where the surface of the bodies conform exactly. Stronge [29] showed that contact models with compliance in the normal and tangential direction to the contact surface area provide a good prediction of experimental results for non-collinear and/or oblique impacts. In this section, novel models using compliance in the normal contact force and the tangential friction force will be presented. Defining $\mathbf{n}$ as the outward unit vector normal to the contact area, the contact force $\mathbf{f}_c$ is decomposed into normal $\mathbf{f}_n$ and tangential $\mathbf{f}_t$ components:

$$\mathbf{f}_c = \mathbf{f}_n + \mathbf{f}_t = f_n \mathbf{n} + \mathbf{f}_t, \tag{1}$$

where the magnitude of the normal force is f_n. Similarly, we define the relative velocity $\mathbf{v}_r$ at a contact point in terms of its normal and tangential components $\mathbf{v}_n$ and $\mathbf{v}_t$ as

$$\mathbf{v}_r = \mathbf{v}_n + \mathbf{v}_t, \tag{2}$$

where

$$\begin{aligned} \mathbf{v}_n &= \mathbf{n}\,(\mathbf{n} \cdot \mathbf{v}_r) = \mathbf{n}\, v_n, \\ \mathbf{v}_t &= (\mathbf{n} \times \mathbf{v}_r) \times \mathbf{n} = \mathbf{v}_r - (\mathbf{v}_r \cdot \mathbf{n})\,\mathbf{n}, \end{aligned} \tag{3}$$

and the magnitude of the normal velocity is v_n.

2.1. NORMAL FORCE MODEL

The compliant normal-force model proposed by Hunt–Crossley for direct central and frictionless impacts is a non-linear spring-damper model of the form

$$f_{\mathrm{n}} = -(\lambda\, x^p)\, \dot{x} - k\, x^p, \tag{4}$$

where x and $\dot{x} = v_{\mathrm{n}}$ are the penetration depth and speed, λ is the 'hysteresis damping factor' and k is the spring constant. In Section 3, it is shown how x and $\mathbf{v}_{\mathrm{r}}$ are computed for a given geometric pair. The force approach law based on Hertzian theory yields $p = 3/2$ when the two contacting bodies are linearly elastic spheres. Non-linear spring models for other geometric pairs have been derived [13]. If the colliding bodies i and j have a mass m_i and m_j, respectively, then the effective mass m can be obtained from $m^{-1} = m_i^{-1} + m_j^{-1}$ [18]. Defining the damping factor a by $\lambda = a\, k$, the equation of relative motion can be written as

$$m\, \dot{v}_{\mathrm{n}} + k\, x^p\, (1 + a\, v_{\mathrm{n}}) = 0. \tag{5}$$

To prevent the contact model from applying tensile forces, a must be selected such that

$$1 + a\, v_{\mathrm{n}} \geq 0 \quad \forall\, v_{\mathrm{n}}. \tag{6}$$

As Marhefka and Orin [24] and Stronge [29] showed, Equation (5) is separable and can be integrated over the impact phase as follows

$$\int_{v_{\mathrm{i}}}^{v_{\mathrm{o}}} \frac{v_{\mathrm{n}}}{1 + a\, v_{\mathrm{n}}}\, \mathrm{d}v_{\mathrm{n}} + \frac{k}{m} \int_{x_{\mathrm{i}}}^{x_{\mathrm{o}}} x^p\, \mathrm{d}x = 0, \tag{7}$$

where x_{i}, x_{o}, v_{i} and v_{o} are the penetration depths and velocities at the start and end of the impact phase. Noting that $x_{\mathrm{i}} = x_{\mathrm{o}} = 0$, the second term of Equation (7) is zero. Hence, v_{o} depends exclusively on v_{i} and a, and is independent of the system's effective mass, stiffness, or the type of spring model used.

To get a better understanding of the relationship between v_{i}, v_{o} and a, we define the effective coefficient of restitution for the contact model e_{eff} as

$$e_{\mathrm{eff}} = -v_{\mathrm{o}}/v_{\mathrm{i}}. \tag{8}$$

Substituting $v_{\mathrm{o}} = -e_{\mathrm{eff}}\, v_{\mathrm{i}}$ into Equation (7) and integrating, yields

$$a\, v_{\mathrm{i}} - \ln(1 + a\, v_{\mathrm{i}}) + e_{\mathrm{eff}}\, a\, v_{\mathrm{i}} + \ln(1 - e_{\mathrm{eff}}\, a\, v_{\mathrm{i}}) = 0. \tag{9}$$

Since a and v_{i} always appear together in Equation (9), a dimensionless factor d defined as $d = a\, e_{\mathrm{eff}}\, v_{\mathrm{i}}$ is introduced and a relationship for d and e_{eff} independent of v_{i} is obtained. The solution to Equation (7) simplifies to

$$\frac{1 + d/e_{\mathrm{eff}}}{1 - d} = \mathrm{e}^{d(1+1/e_{\mathrm{eff}})}. \tag{10}$$

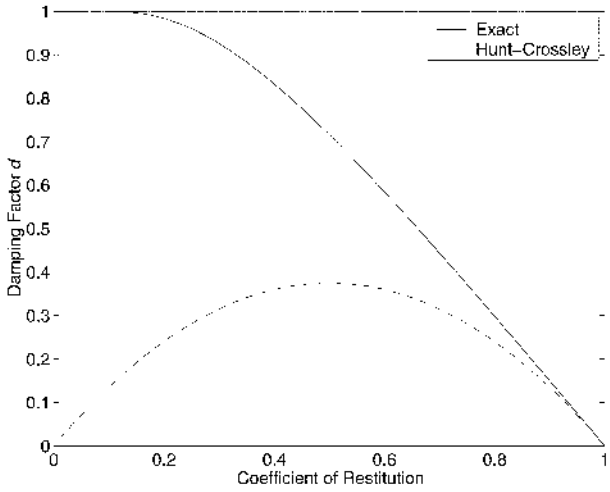

Figure 1. Damping factor d as a function of e_{eff}.

Since d is a function of e_{eff} only, $a\ v_{\text{i}} = d/e_{\text{eff}}$ is also a function of e_{eff} only. Thus, the damping factor a is always inversely proportional to v_{i} (and v_{o}) for any e_{eff}, and for any impact velocity.

The solution for Equation (10) has multiple branches (one of them being $d = 0$). However, a valid solution for this problem should be such that Equation (6) is satisfied. Noting that $v_{\text{i}} < v_{\text{n}} < -e_{\text{eff}}\, v_{\text{i}}$ (for $v_{\text{i}} < 0$), we conclude that the valid solution branch for d will be such that $d \leq 1$ for any e_{eff}.

Figure 1 shows the corresponding solution branch for d. Clearly, d is always less than or equal to 1 and goes to zero at $e_{\text{eff}} = 1$. The solution can be obtained by solving Equation (10) with a numerical bisection algorithm. A good initial guess, $d_{\text{est}} = 1 - e_{\text{eff}}^2$ is provided. Since the relationship between e_{eff} and d is constant, the solution can be found a-priori and does not need to be computed during the simulation. This branch uniquely defines the damping factor d as a function of e_{eff}. The hysteresis damping factor is now expressed as

$$\lambda = \frac{k\, d}{e_{\text{eff}}\, v_{\text{i}}}. \tag{11}$$

Equation (11) predicts that λ will become very large as e_{eff} becomes small, an observation that is consistent with the need to have high energy dissipation in plastic impacts.

It has been shown that at low impact velocities and for most linear materials with an elastic range [9], the coefficient of restitution can be approximated by

$$e_{\text{emp}} = 1 - \alpha\, v_{\text{i}}, \tag{12}$$

where α is an empirically determined constant that is valid for a limited range of impact velocities. For steel, bronze or ivory, α is equal to 0.08. . .0.32 s/m. Using

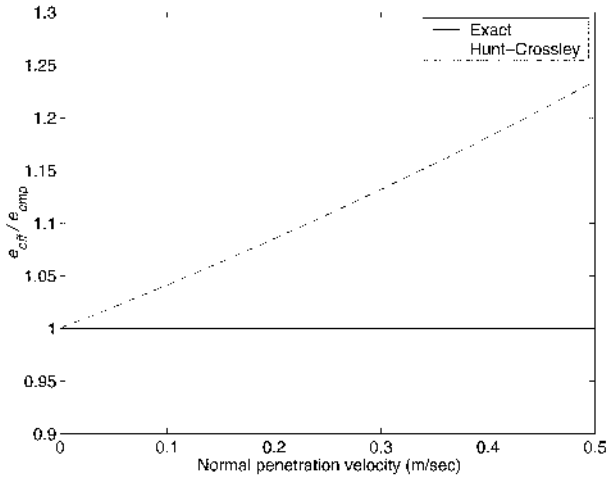

Figure 2. Effective coefficient of restitution for two models of d (mass: 0.454 kg; $k = 3.4 \cdot 10^{10}$ N/m$^{3/2}$; $\alpha = 0.2$ s/m).

the definition of e_{emp} and some simplifying assumptions, Hunt and Crossley [11] and Marhefka and Orin [24] derived a simpler formula for λ

$$\lambda_{\text{HC}} = \frac{3}{2}\alpha k. \tag{13}$$

A definition d_{HC} corresponding to the model proposed by Hunt and Crossley can be obtained by setting Equation (11) equal to Equation (13) and replacing α using Equation (12), resulting in

$$d_{\text{HC}} = \frac{3}{2}e_{\text{eff}}\,(1 - e_{\text{eff}}). \tag{14}$$

Figure 1 shows that the Hunt and Crossley definition for d approximates the exact solution only in the region where e_{eff} is near unity.

Figure 2 shows the ratio of e_{eff} to e_{emp} obtained using the model proposed by Hunt and Crossley [11] for the impact of a sphere on a plane, and the model proposed here as a function of impact velocity, with $\alpha = 0.2$ s/m. Clearly, the model proposed here yields a dynamic behavior that is consistent with any given value of the coefficient of restitution. Hence, the model can also be used for plastic impacts, given that a function for the coefficient of restitution is provided. The model proposed by Hunt and Crossley [11] is consistent with the given coefficient of restitution only when $v_{\text{i}} = 0$ (and $e = 1$ from Equation (12)), i.e. for perfectly elastic impacts.

Stoianovici and Hurmuzlu [28] tuned the damping factor to obtain a good match between experimental and simulated results of a beam impacting a hard surface, without formal knowledge of the exact relationship between λ and e_{eff}. Instead, they arbitrarily varied λ to get the best possible match. The damping factor thus

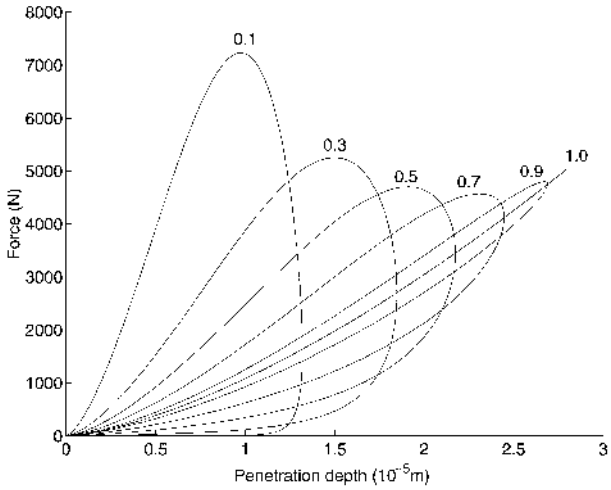

Figure 3. Contact force vs. indentation for various values of e_{eff} (mass: 0.454 kg; $k = 3.4 \cdot 10^{10}$ N/m$^{3/2}$).

identified approximates the experimental behavior only in the range of normal impact velocities used in the experiment. The damping factor model proposed here is not subject to this limitation, since v_{i} can be varied over a wide range, without reducing the accuracy of the approximation, as shown in Figure 2.

Figure 3 shows the contact force profile as a function of indentation depth for the same sphere-plane impact, for various restitution coefficients ranging from 0.1 to 1. Notice that, at large values of the restitution coefficient, the damping in the compression and restitution phase is essentially symmetric. On the other hand, for low values of e_{eff} most of the energy (area inside the curve) is dissipated in the compression phase and the hysteretic damping becomes asymmetric.

2.2. TANGENTIAL FRICTION MODEL

While the damping in the normal contact force is a significant phenomenon through which energy is dissipated during the impact phase, we must also consider the effects of the friction acting along the surface of the contacting bodies in the region of contact.

Unlike the derivation done in the previous section, where the magnitude of the normal contact force was derived using scalar equations, the surface friction force is a vectorial quantity by nature. For oblique and/or non-collinear impacts, the dynamics of motion will in general be coupled in all directions. Thus, it would be incorrect to use two independent, one-dimensional friction models for the friction forces acting along a two-dimensional surface. Furthermore, the stick-slip transitions cannot be considered in the context of an arbitrary direction, e.g. when two colliding bodies are moving with respect to each other; they cannot be sticking in one direction, and sliding in another.

Canudas de Wit et al. [6] introduced a one-dimensional dynamic friction model that combines the stick-slip behavior and Stribeck effects, which is characterized by decreasing friction with increasing velocity at low velocity [2]. To model these frictional effects, it is postulated that the two rigid bodies make contact through elastic bristles. The friction force is modeled as a function of the bristle deformation z and deformation rate $\dot{z}$. The bristle state is defined at the velocity level, and integrated to obtain local deformation. This model can be transformed into a vectorized friction model by simply expressing the bristle deformation z as a vectorial quantity, $\mathbf{z}$, without affecting the model properties. The friction force generated from the bending of the bristles is described as

$$\mathbf{f}_{\mathrm{br}} = \sigma_{\mathrm{o}}\,\mathbf{z} + \sigma_1\,\dot{\mathbf{z}}, \tag{15}$$

where σ_{o} is the stiffness and σ_1 is a damping coefficient. However, the use of this model results in ordinary differential equations (ODEs) that are very stiff at low relative velocities (i.e. small $\mathbf{v}_{\mathrm{t}}$), and cannot be solved using explicit ODE solvers. The bristle state dynamics can be shown to have a time constant of $1/|\mathbf{v}_{\mathrm{t}}|$, which becomes very large at low velocities, while the time constant associated with the relative body motion dynamics are small and constant during stick.

A new definition for the bristle state is therefore needed. To this end, the bristle dynamics model for $\dot{\mathbf{z}}$ is reformulated into two distinct sub-models: $\dot{\mathbf{z}}_{\mathrm{st}}$ for the sticking regime and $\dot{\mathbf{z}}_{\mathrm{sl}}$ for the sliding regime. A sticking state function s is introduced to transition smoothly between the stick-slip friction regimes. The deformation rate is now expressed as

$$\dot{\mathbf{z}} = s\,\dot{\mathbf{z}}_{\mathrm{st}} + (1 - s)\,\dot{\mathbf{z}}_{\mathrm{sl}}, \tag{16}$$

where

$$s = \mathrm{e}^{-(\mathbf{v}_{\mathrm{t}}\cdot\mathbf{v}_{\mathrm{t}})/(v_{\mathrm{S}}^2)}, \tag{17}$$

and v_{S} is the velocity at which the Stribeck effect occurs. With this formulation, $\dot{\mathbf{z}}$ becomes $\dot{\mathbf{z}}_{\mathrm{st}}$ (sticking case) when $\mathbf{v}_{\mathrm{t}}$ approaches zero, i.e., $(1 - s) \rightsquigarrow 0$. If $\mathbf{v}_{\mathrm{t}}$ increases, $\dot{\mathbf{z}}$ becomes $\dot{\mathbf{z}}_{\mathrm{sl}}$ (sliding case), i.e., $s \rightsquigarrow 0$.

When the friction state is in the stiction regime, the relative motion of the bristles should match exactly the relative motion of the rigid bodies, i.e. the surfaces stick together. Hence, $\dot{\mathbf{z}}_{\mathrm{st}}$ is defined as

$$\dot{\mathbf{z}}_{\mathrm{st}} = \mathbf{v}_{\mathrm{t}}. \tag{18}$$

The sliding rate $\dot{\mathbf{z}}_{\mathrm{sl}}$ is defined in terms of the Coulomb friction force $\mathbf{f}_{\mathrm{C}}$ that acts while the two bodies are sliding with respect to each other. Coulomb friction acts in a direction opposite to the relative velocity $\mathbf{v}_{\mathrm{t}}$ between the two bodies and its magnitude is $\mu_{\mathrm{C}}\,f_{\mathrm{n}}$, where μ_{C} is the Coulomb friction coefficient. The friction force $\mathbf{f}_{\mathrm{C}}$ is thus described by

$$\mathbf{f}_{\mathrm{C}} = \mu_{\mathrm{C}}\,f_{\mathrm{n}}\,\mathrm{dir}_{\epsilon}(\mathbf{v}_{\mathrm{t}}, v_{\epsilon}), \tag{19}$$

where $\mathrm{dir}_\epsilon(\mathbf{v}_\mathrm{t}, v_\epsilon)$ returns a unit vector along the direction of $\mathbf{v}_\mathrm{t}$ and uses the relaxed sign convention near a small velocity tolerance v_ϵ:

$$\mathrm{dir}_\epsilon(\mathbf{v}_\mathrm{t}, v_\epsilon) = \begin{cases} \frac{\mathbf{v}_\mathrm{t}}{|\mathbf{v}_\mathrm{t}|}; & |\mathbf{v}_\mathrm{t}| \geq v_\epsilon, \\ \frac{\mathbf{v}_\mathrm{t}}{v_\epsilon}\left(\frac{3}{2}\cdot\frac{|\mathbf{v}_\mathrm{t}|}{v_\epsilon} - \frac{1}{2}\left(\frac{|\mathbf{v}_\mathrm{t}|}{v_\epsilon}\right)^3\right); & |\mathbf{v}_\mathrm{t}| < v_\epsilon. \end{cases} \tag{20}$$

While the two rigid bodies are sliding with respect to each other, the friction force $\mathbf{f}_\mathrm{br}$ applied by the bristle should be $\mathbf{f}_\mathrm{C}$. Setting Equation (15) equal to Equation (19), and solving for $\dot{\mathbf{z}} \approx \dot{\mathbf{z}}_\mathrm{sl}$,

$$\dot{\mathbf{z}}_\mathrm{sl} = \frac{1}{\sigma_1}\mathbf{f}_\mathrm{C} - \frac{\sigma_\mathrm{o}}{\sigma_1}\mathbf{z}. \tag{21}$$

Equation (21) is a first order ODE and has a time constant $\tau_\mathrm{br} = \sigma_1/\sigma_\mathrm{o}$. The bristle dynamics time constant τ_br controls how fast the bristles reach a steady-state deformation when two rigid bodies are moving at a constant relative velocity. To summarize, the bristle deformation rate is given as

$$\dot{\mathbf{z}} = s\,\mathbf{v}_\mathrm{t} + (1-s)\left(\frac{1}{\sigma_1}\mathbf{f}_\mathrm{C} - \frac{\sigma_\mathrm{o}}{\sigma_1}\mathbf{z}\right). \tag{22}$$

While the two rigid bodies are sticking to each other, the maximum friction force is limited by the stiction force $\mu_\mathrm{S}\, f_\mathrm{n}$, where μ_S is the stiction coefficient. Experimental observations [26, 4] have shown that the full magnitude of the stiction force does not come into effect as soon as the relative velocity becomes zero. Instead, the maximum stiction force gradually increases over time, and eventually reaches the upper limit $\mu_S\, f_\mathrm{n}$. This phenomenon is also called dwell-time dependency.

On the other hand, the temporal lag effect associated with the dwell-time is only present for the slip-stick transition, i.e. it takes some time for the microscopic asperities to settle into each other and for the molecular bonding to take place. As soon a stick-slip transition occurs, these bonds shatter at once. Hence, there is a need to include two time constants to correctly model the dwell-time effect on the maximum stiction force. A new state, s_dw, is introduced to model the effect of the dwell-time on the maximum stiction force

$$\dot{s}_\mathrm{dw} = \begin{cases} \frac{1}{\tau_\mathrm{dw}}(s - s_\mathrm{dw}); & s - s_\mathrm{dw} \geq 0, \\ \frac{1}{\tau_\mathrm{br}}(s - s_\mathrm{dw}); & s - s_\mathrm{dw} < 0, \end{cases} \tag{23}$$

where τ_dw is the dwell-time dynamics time constant and τ_br is the bristle dynamics time constant, as before. With the definition proposed for $\dot{s}_\mathrm{dw}$ in Equation (23), s_dw simply follows the value of s with a long time delay as s goes to 1 (sticking) while it follows it very quickly (as fast as the bristle dynamics allow) when s goes to zero (sliding). The maximum stiction force f_max can now be defined as

$$f_\mathrm{max} = f_n(\mu_\mathrm{C} + (\mu_\mathrm{S} - \mu_\mathrm{C})s_\mathrm{dw}). \tag{24}$$

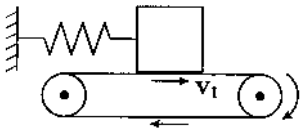

Figure 4. The Bowden and Leben stick-slip experimental apparatus.

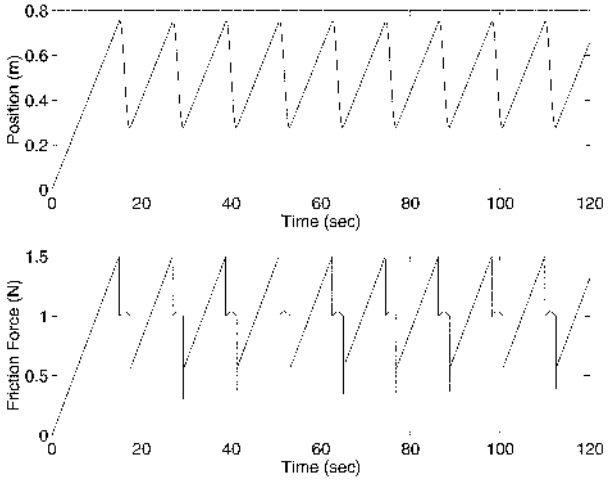

Figure 5. Bowden and Leben stick-slip experiment for $|\mathbf{v}_t| = 0.05$ m/s.

As mentioned previously, the bristle friction force should never exceed $f_{\max}$ at any time. In particular, the stick-slip friction regime transition can only happen if the magnitude of the bristle force becomes saturated, such that the surfaces of the two rigid bodies can start accelerating with respect to each other and the relative velocity increases beyond v_S. To this end, we introduce the saturation function $\text{sat}(\mathbf{f}_{br}, f_{\max})$

$$\text{sat}(\mathbf{f}_{br}, f_{\max}) = \begin{cases} \mathbf{f}_{br}; & |\mathbf{f}_{br}| \leq f_{\max}, \\ \dfrac{\mathbf{f}_{br}}{|\mathbf{f}_{br}|} f_{\max}; & |\mathbf{f}_{br}| > f_{\max}. \end{cases} \tag{25}$$

The tangential friction force $\mathbf{f}_t$ can now be computed. A term proportional to the relative tangential velocity is added to account for viscous friction so that

$$\mathbf{f}_t = -(\text{sat}(\mathbf{f}_{br}, f_{\max}) + \sigma_2 \mathbf{v}_t), \tag{26}$$

where σ_2 is the viscous damping coefficient. Hence, the proposed friction model is a seven parameter model. These parameters are: μ_S , μ_C, σ_o, σ_1, σ_2, v_S and τ_{dw}. Note that the bristle dynamics time constant is inferred from σ_o and σ_1, and a numerical tolerance v_ϵ must also be specified. As a guideline the v_ϵ should be at most one tenth of v_S. In all following experiments a value of $v_\epsilon = 1/100\ v_S$ is used.

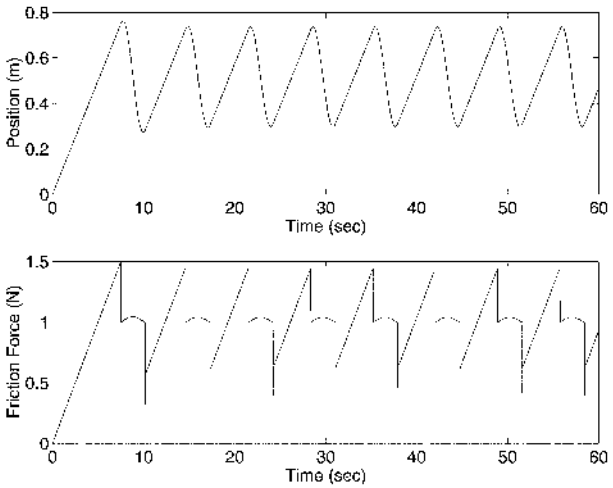

Figure 6. Bowden and Leben stick-slip experiment for $|\mathbf{v}_t| = 0.1$ m/s.

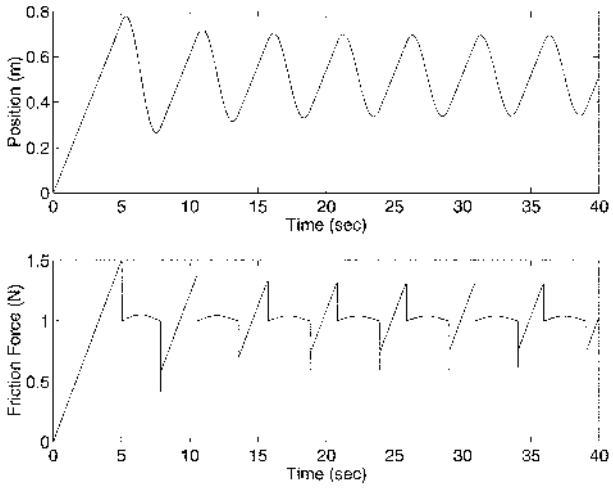

Figure 7. Bowden and Leben stick-slip experiment for $|\mathbf{v}_t| = 0.15$ m/s.

Table I. Numerical values for Bowden and Leben stick-slip experiment.

μ_S	μ_C	σ_0	σ_1	σ_2	v_S	τ_{dw}
0.15	0.1	10^5 N/m	$\sqrt{10^5}$ Ns/m	0.1 Ns/m	0.001 m/s	2 s

Using the parameters given in Table I, the friction model was used to simulate the response of a spring-mounted block sitting on a plate that is moved at a constant speed as shown in Figure 4. This experiment was first proposed by Bowden and Leben who built an apparatus to study the stick-slip process [26].

To test our vectorized model, the motion direction is at 45 deg from the x-axis in the x–y plane, moving away from the origin, the spring constant is $k = 2$ N/m, the mass $m = 1$ kg and the gravitational constant is 10 m/s^2. The block sticks to the plate until the spring force is high enough to overcome the friction force, at which point the block slides in the opposite direction to the plate. The results are plotted in Figures 5–7 for three different speeds of the plate. The position axes show the distance from the origin and the force axes correspond to the magnitude of the friction force.

Note the sharp spikes in the friction curves corresponding to transitions between forward and reverse velocities of the block. When the plate is moving slowly, the position curve drops almost vertically as soon as the block starts sliding. Then, as the plate moves faster the amplitude of the oscillations decreases, and the profile becomes similar to a sinusoidal wave. However, in all cases, the first peak of the friction profiles always extends up to the maximum stiction limit, a consequence of the dwell-time dynamics (the friction model is initialized in the 'sticking' state). Subsequent peaks are of lesser magnitude for higher speeds of the plate, because there is not enough time for the stiction force to reach its maximum value of $\mu_S f_n$. This dynamic behavior corresponds to the observations by Rabinowicz [26].

3. Contact Model Implementation

The contact model derived in the previous section computes the contact forces between two non-conforming rigid bodies as a function of the relative velocity $\mathbf{v}_r$ in the contact region, and the penetration depth x. In addition, the point of application of the contact force is required. Note that the contact region is assumed to be very small, so the moments generated by the local deformations in the contact region are neglected. This section will demonstrate how to set up the proposed contact model for the simulation of collision between two rigid bodies with arbitrary non-conforming shapes. The case of the sphere-plane pair will be presented as an example.

For a given non-conforming geometric pair, a *point of action* $\mathbf{p}_a$ is defined as the point where the equal and opposite contact forces are applied to the two bodies. In the case of the sphere-plane pair, the Hertz force approach law is based on the deepest penetration distance. The point of action is selected as the point along the sphere surface at which the sphere surface normal is exactly opposite to the plane normal. This choice is convenient since by measuring the height of the point of action with respect to the plane surface, the desired penetration distance is obtained.

We describe the states of two arbitrary bodies i and j by defining body-fixed frames $\mathcal{K}_i$ and $\mathcal{K}_j$. Each frame origin is located by the position vectors $\mathbf{r}_i$ and

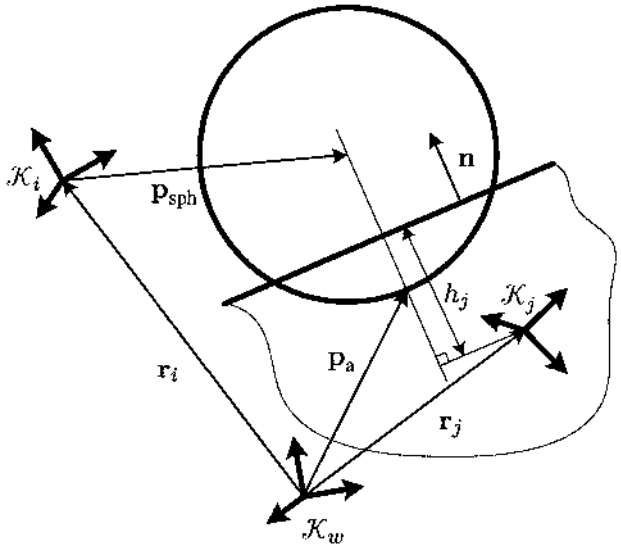

Figure 8. Point of action and penetration depth for a sphere-plane pair.

$\mathbf{r}_j$ relative to an inertial 'world' frame $\mathcal{K}_w$. Their orientation is assumed to be described by the rotation matrices $\boldsymbol{R}_i$ and $\boldsymbol{R}_j$. The frames translate at a velocity $\mathbf{v}_i$ and $\mathbf{v}_j$ and rotate with an angular velocity $\boldsymbol{\omega}_i$ and $\boldsymbol{\omega}_j$.

For the sphere-plane example, the position of the center of the sphere (i) with respect to $\mathcal{K}_i$ is $\mathbf{p}_{\text{sph}}$, and the sphere radius is R. The surface of the plane (j) is located at a height h_j along the plane normal $\mathbf{n}$ from the origin of $\mathcal{K}_j$, see Figure 8. In the following derivations, all vectorial quantities are assumed to be expressed in $\mathcal{K}_w$. Typically, $\mathbf{p}_{\text{sph}}$ and $\mathbf{n}$ are specified in local frame coordinates by the user, but they can be easily transformed into $\mathcal{K}_w$ by using $\boldsymbol{R}_i$ and $\boldsymbol{R}_j$.

In the case of the sphere-plane geometric pair, the point of action is found as follows:

$$\mathbf{p}_{\text{a}} = \mathbf{r}_i + \mathbf{p}_{\text{sph}} - R\,\mathbf{n}. \tag{27}$$

The height x of the point of action with respect to the plane is given by

$$x = (\mathbf{p}_{\text{a}} - \mathbf{r}_j) \cdot \mathbf{n} - h_j, \tag{28}$$

which is the expression for the penetration depth needed to evaluate Equation (4). This same expression can be used to detect contact, i.e. when $x < 0$, so a separate collision detection algorithm is not needed for this case.

In the general case, $\mathbf{p}_{\text{a}}$ must first be identified using a collision detection algorithm. Then, $\mathbf{p}_{\text{a}}$ is arbitrarily assumed to belong to one of the bodies, say body i, after which the surface normal $\mathbf{n}$ and height h to the surface of the other body j can be found as a function of $(\mathbf{p}_{\text{a}} - \mathbf{r}_j)$.

The relative velocity at the point of action is given by

$$\mathbf{v}_{\text{r}} = \mathbf{v}_i + \boldsymbol{\omega}_i \times (\mathbf{p}_{\text{a}} - \mathbf{r}_i) - \mathbf{v}_j - \boldsymbol{\omega}_j \times (\mathbf{p}_{\text{a}} - \mathbf{r}_j). \tag{29}$$

Table II. Numerical values for the bouncing ball experiments.

μ_S	μ_C	σ_o	σ_1	σ_2	v_S	τ_{dw}
0.45	0.4	10^5 N/m	10^4 Ns/m	0 Ns/m	0.1 m/s	0.01 s

The contact force $\mathbf{f}_c$ is then computed by substituting Equations (28) and (29) into Equations (3), (4) and (26). Since $\mathbf{f}_c$ is a function of the states s and $\mathbf{z}$, Equations (22) and (23) are added to the set of original system of ODEs.

Note that there is no need to convert the contact model input data into normal and tangential components with respect to the surface. The vectorized friction model automatically generates a friction force along the direction of tangential displacement. Although, $\mathbf{f}_t$ acts in the tangential plane, it is a vectorial quantity that can be resolved in any frame of reference, here $\mathcal{K}_w$. The same holds true for $\mathbf{f}_n$. Hence, $\mathbf{f}_t$ can be directly added to $\mathbf{f}_n$ as in Equation (1).

A useful feature of the proposed contact model is that it can be directly applied to model contact between bodies that are rolling with respect to each other. Since the input to the friction model is the relative tangential velocity between the two contacting surfaces, the bristle model will integrate over time the motion of the point of action. In effect, the friction model "tracks" the point of action, which is moving with respect to both bodies.

Once the force generated from the local surface deformations has been computed, its contribution to the body forces $\mathbf{f}_{i,j}$ and moments $\boldsymbol{\tau}_{i,j}$ acting on each body are given by

$$\begin{aligned} \mathbf{f}_i &= \mathbf{f}_c; \quad \boldsymbol{\tau}_i = (\mathbf{p}_a - \mathbf{r}_i) \times \mathbf{f}_c, \\ \mathbf{f}_j &= -\mathbf{f}_c; \quad \boldsymbol{\tau}_j = -(\mathbf{p}_a - \mathbf{r}_j) \times \mathbf{f}_c. \end{aligned} \tag{30}$$

The proposed contact model adds little computational overhead to the multibody dynamics simulation since Equations (4) and (26) are simple explicit expressions, and thus it is suitable for a real-time implementation. For the case of arbitrary geometries, the only extra computational effort will be focused on finding the location of the contact points and the penetration depths, the determination of which has been intensely investigated in the past decade, and for which very efficient algorithms are available [12, 21].

4. Numerical Examples

4.1. A BOUNCING BALL

A simulation model was implemented for a 2 kg ball, with 0.1 m radius, colliding with an inclined plane. From the horizontal position, the plane is rotated 20 deg about the $+Y$ axis. Gravity $g = 9.81$ m/s^2 acts in the $-Z$ direction. The ball

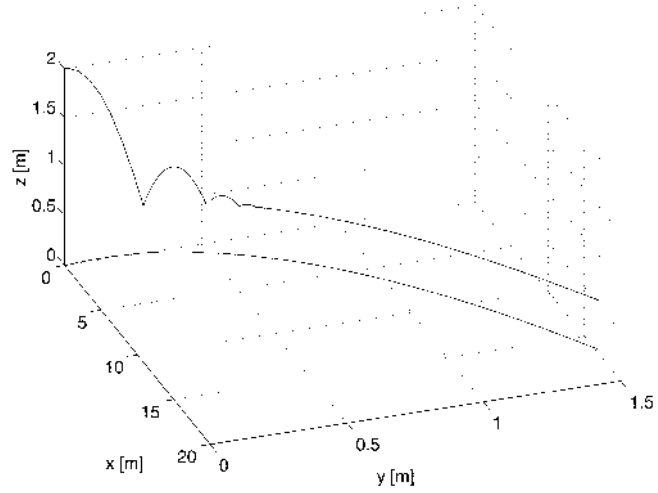

Figure 9. Trajectory of sphere impacting an inclined plane.

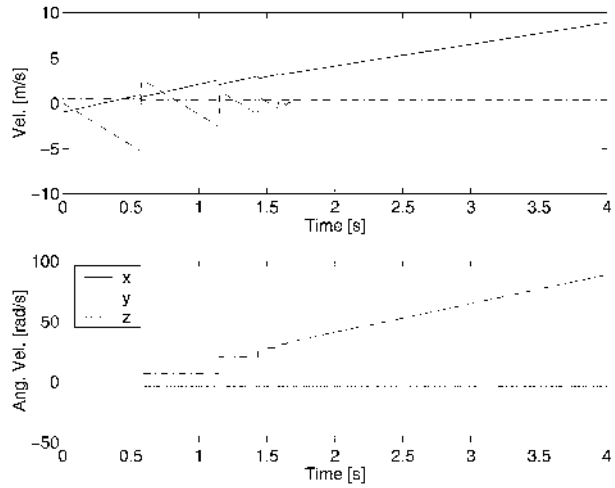

Figure 10. Velocity components versus time.

is given an initial velocity of -1 m/s in the X direction and 0.5 m/s in the Y direction. The normal impact model with $k = 10^6$ N/m$^{3/2}$ was set to have a constant coefficient of restitution of 0.5. The friction model parameters are shown in Table II.

Figure 9 shows the three-dimensional trajectory of the ball center, plotted in a xyz frame that is rotated with the plane. Thus, once the state of pure rolling has been reached, the only acceleration is $g \sin 20$ in the local x direction. The x and y components of the path are projected onto the $z = 0$ plane. Figure 10 shows the corresponding velocity profiles. Note that when pure rolling occurs (zero z velocity), the velocity in the y direction remains constant while the x component increases

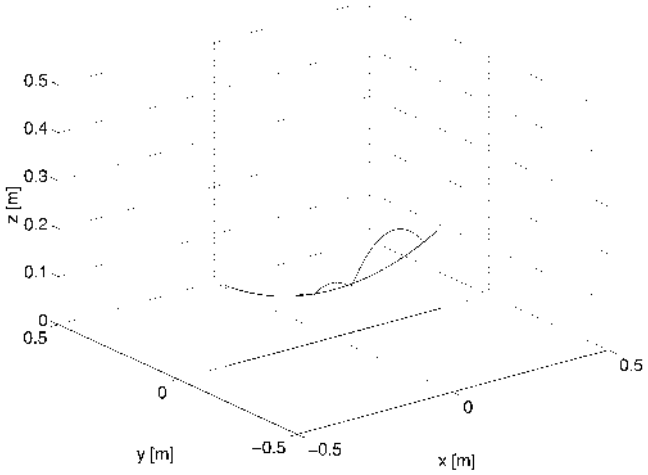

Figure 11. Trajectory of sphere impacting a cylinder (2D motion).

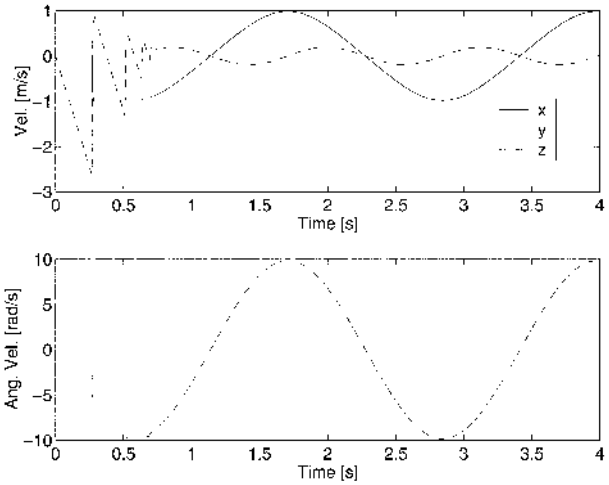

Figure 12. Velocity components versus time.

linearly, as expected. Note also that the angular velocities remain constant, except for the component in the y direction, which also increases linearly in agreement with $|\mathbf{v}| = R|\boldsymbol{\omega}|$. It is seen that the two motions are coupled by the friction force which imposes a no-slip condition.

The same ball was then dropped on the inside surface of a 1 m radius cylinder aligned in the Y direction. The ball was given an initial offset from the cylinder axis of 0.3 m in the X direction so that the first impact will cause motion in the X–Z plane only.

Figure 11 shows the resulting three-dimensional trajectory of the ball center. The X and Y components of the trajectory are shown below in the $Z = 0$ plane. Note the ball oscillations inside the cylinder. Figure 12 shows the velocity profiles.

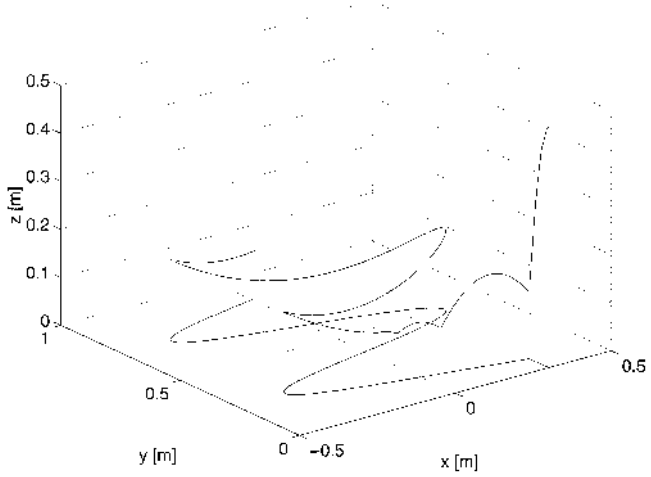

Figure 13. Trajectory of sphere impacting a cylinder (3D motion).

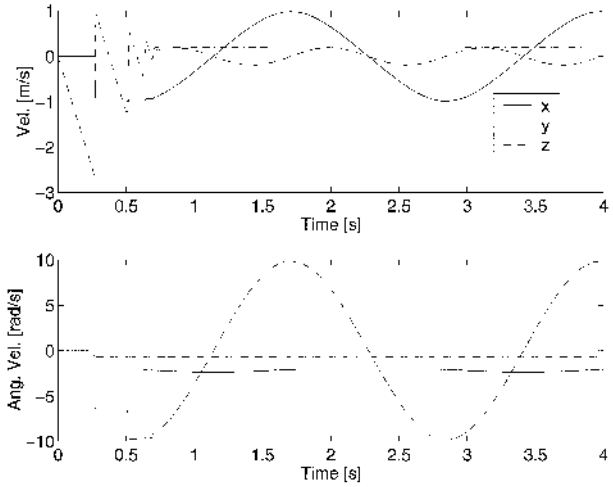

Figure 14. Velocity components versus time.

The angular velocity in the Y direction oscillates, while the other angular velocity components are zero. Again, there is coupling between the translational and rotational motions through the effect of the friction. See also that the model changes the orientation of the friction force to correctly impose the no-slip condition. It is easy to verify that $|\mathbf{v}| = R|\boldsymbol{\omega}|$ during the rolling motion, e.g. $|\mathbf{v}| = 1$ m/s when $|\boldsymbol{\omega}|$ peaks at 10 rad/s.

The same experiment was then conducted, but this time the ball is given an initial velocity of 0.3 m/s in the Y direction.

Figure 13 shows the trajectory of the ball center, with the X and Y components projected onto the $z = 0$ plane. Note the ball oscillation as it rolls along the cylinder. Figure 14 shows the corresponding velocity profiles. As expected, a non-

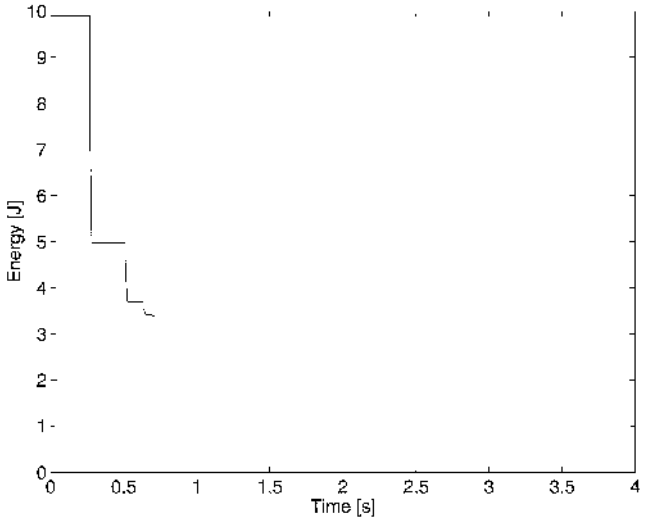

Figure 15. Total energy for 3D motion.

zero angular velocity in the Z direction results from the first impact, while the X component of angular velocity is no longer constant. Note also that the amplitude of the oscillation does not decay with time. This is to be expected since there is no spinning or rolling frictional effects included in the proposed contact model, and the tangential friction force does no work. Figure 15 shows the total energy of the sphere (kinetic and potential) and the contact model spring as a function of time. Clearly, energy is dissipated during the impact phase, but as soon as the sphere settles into pure rolling motion the energy is constant.

4.2. A DOUBLE PENDULUM

Figure 16 shows the schematic diagram of a double pendulum, with a spring placed at the bottom to represent the surface compliance. The tip of the pendulum is allowed to hit the surface located 0.61 m below the first joint axis. The governing equations of motion were obtained using a computer algebra system [19, 27]. The two coupled ODEs and the contact force model are then evaluated and solved numerically within the Simulink simulation environment using the ode3 fixed-step solver.

The initial conditions were selected to give the system high kinetic energy with the tip of the pendulum moving towards the plane. To better illustrate the effects of the contact model on the system's response, the joints are modeled as frictionless. The normal impact model with $k = 10^9$ N/m$^{3/2}$ was set to have a constant coefficient of restitution of 0.9. The friction model parameters are shown in Table III.

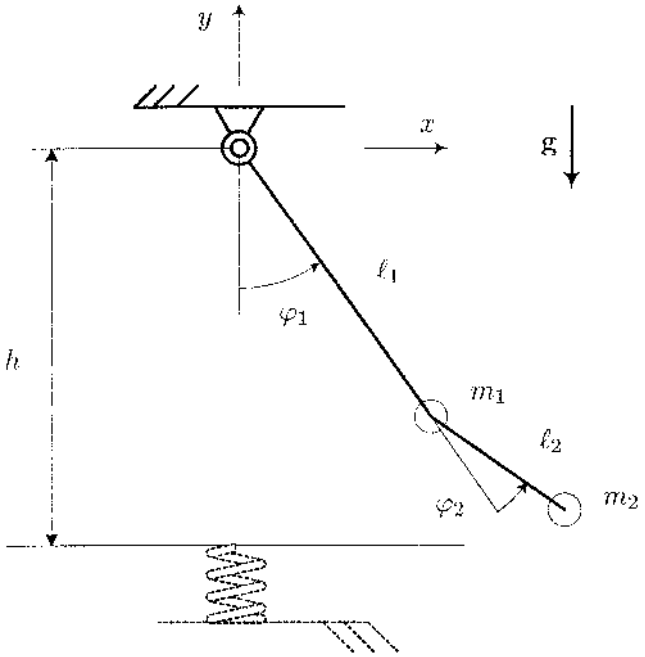

Figure 16. Mechanical test system: double pendulum ($\varphi_{o_1} = 45$ deg, $\varphi_{o_2} = 0$ deg, $\dot{\varphi}_{o_1} = -120$ deg/s, $\dot{\varphi}_{o_2} = 130$ deg/s, $\ell_1 = 0.5$ m, $m_1 = 5.0$ kg, $\ell_2 = 0.25$ m, $m_2 = 2.0$ kg, $g = 9.81$ m/s^2, $h = 0.61$ m).

Table III. Numerical values for double pendulum experiments.

μ_S	μ_C	σ_o	σ_1	σ_2	v_S	τ_{dw}
0.15	0.12	10^5 N/m	$\sqrt{10^5}$ Ns/m	0 Ns/m	0.1 m/s	0.75 s

The resulting joint motion is shown in Figures 17 and 18. The second joint motion first moves into the positive angles region, and finally settles at a negative angle around -65 degs. Figure 19 shows the corresponding tip motion in the x–y plane as it moves from the initial position (marked by a circle) into the bouncing motion. It can be seen that after bouncing several times, the tip settles into a slowly decaying oscillatory motion in x. Note that if the contact surface had been well lubricated and therefore free of the stick-slip effect, the damping caused by the lubrication would have slowly dissipated the kinetic energy in the system. The final resting position would then be at the equilibrium where $\varphi_1 = 0$ deg since the surface is modeled as being perfectly horizontal. Instead, the stick-slip effect of the tangential friction model causes the final resting position of the first joint to be off-center by 2.2 deg. Figure 20 shows that the friction model switches into the 'sticking mode' after 6.5 s, as s_{dw} goes to 1.

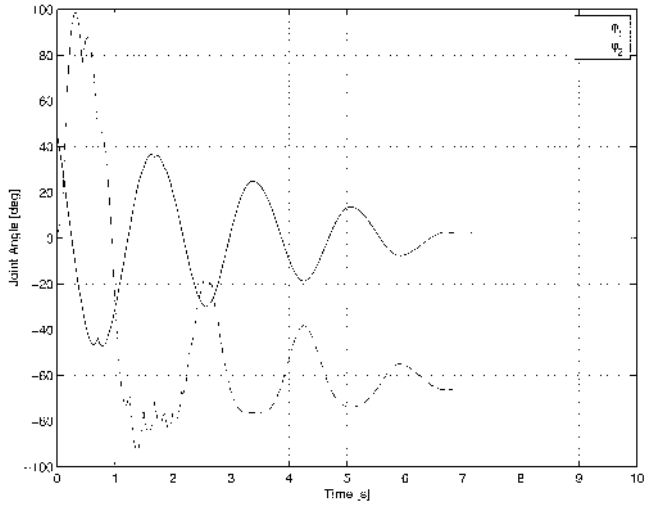

Figure 17. Joint positions.

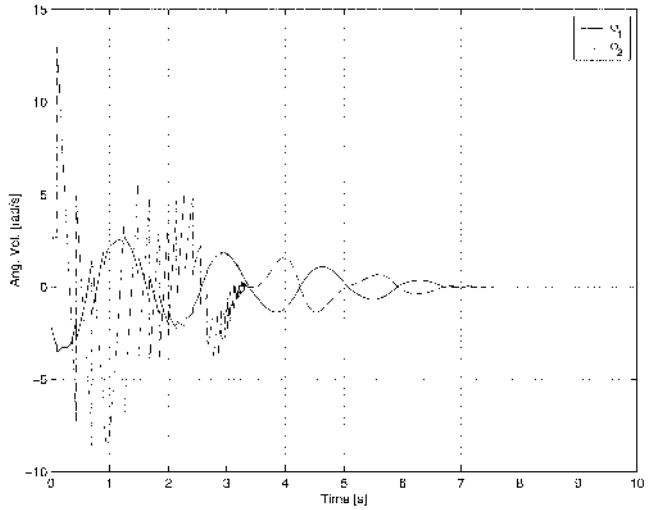

Figure 18. Joint velocities.

Figure 21 shows that the total energy in the system is constant in between collisions, drops rapidly when the tip bounces on the surface and then slowly decays down to a constant value once lasting contact occurs.

The double pendulum model was then modified to match the benchmark simulation model from [1] where $l_1 = l_2 = 1$ m, $m_1 = m_2 = 2$ kg and the link intertia are $J_1 = J_2 = 1/6$ kg m^2. The energy dissipation occurring over a single impact is studied at two pendulum configurations (a) at $\varphi_{o_1} = 18$ deg, $\varphi_{o_2} = 12$ deg, and (b) at $\varphi_{o_1} = 0$ deg, $\varphi_{o_2} = 20.7$ deg. The initial velocities in both cases are $\dot{\varphi}_{o_1} = \dot{\varphi}_{o_2} = -1$ rad/s. The percentage of energy loss is computed for three

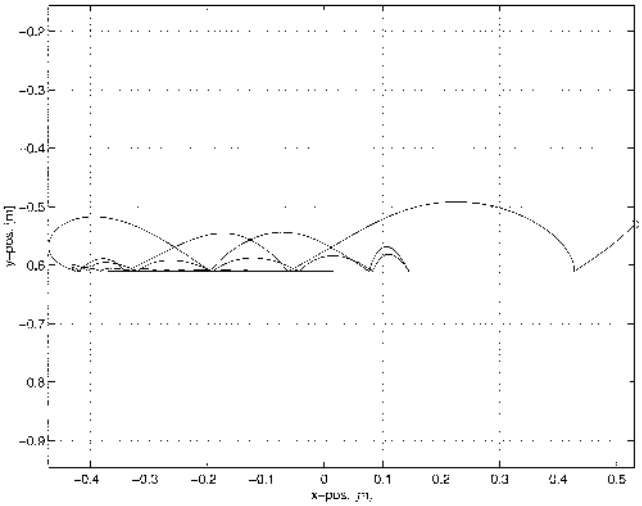

Figure 19. $x-y$ plot of end-effector positions.

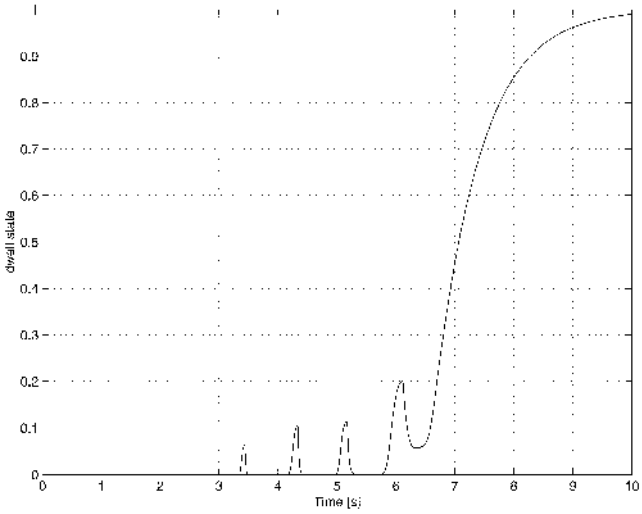

Figure 20. Dwell state s_{dw}.

different values of the coefficient of restitution, as a function of friction coefficient values. In our simulations, the values for μ_{S} and μ_{C} were set equal so that $\mu_{\mathrm{S}} = \mu_{\mathrm{C}} = \mu$, and vary from 0 to 1. The other contact model parameters are the same as before.

The results are shown in Figures 22 and 23 and match perfectly the benchmark results, except for the $e = 0$ case, which cannot be implemented with our restitution model, as this results in a division by 0. For our simulation, $e = 0.01$ was used instead, and the resulting energy dissipation is shown to be very similar to the results for $e = 0$ of the benchmark simulation.

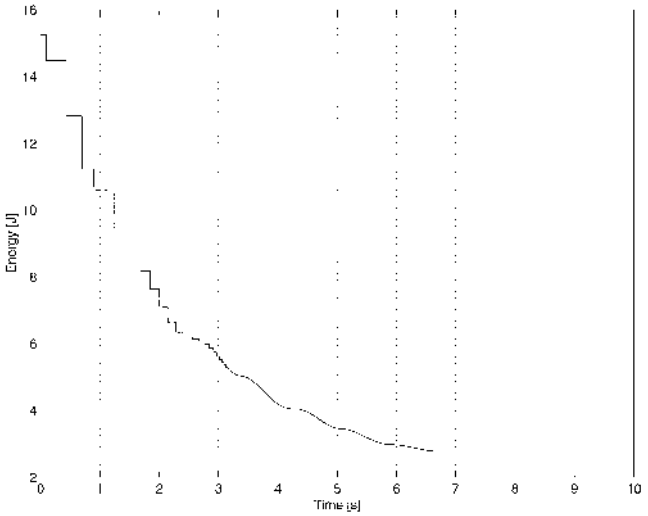

Figure 21. Energy of double pendulum.

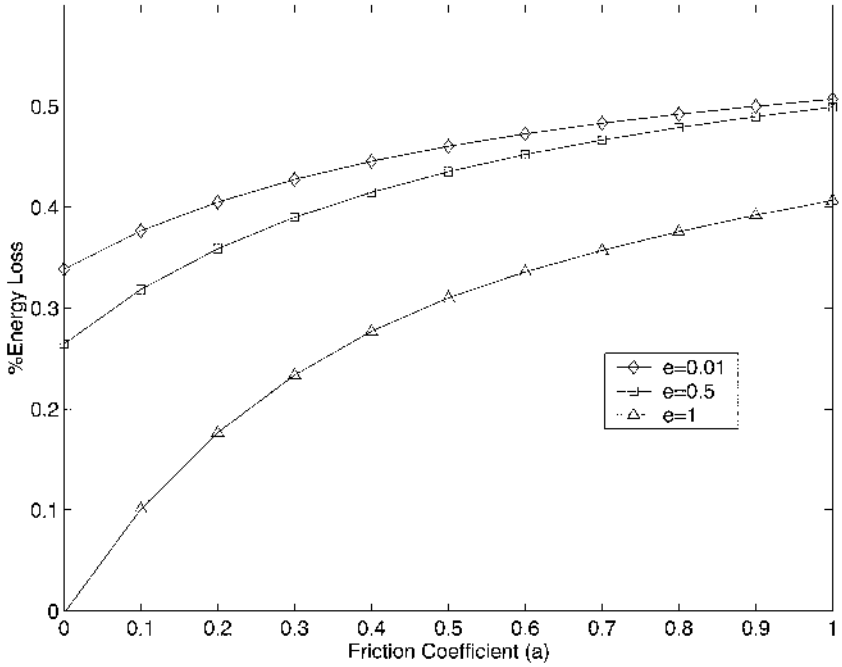

Figure 22. Double pendulum results for case (a).

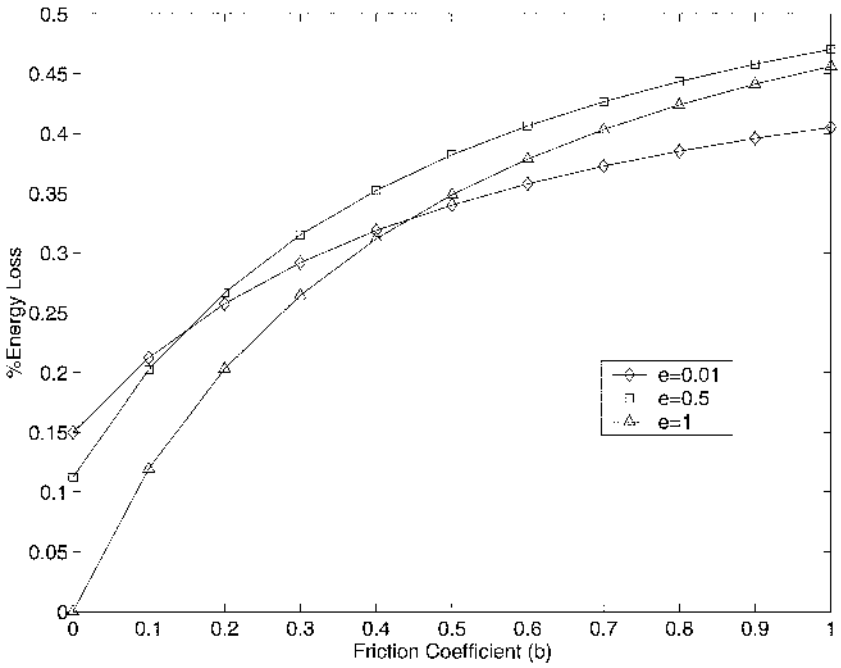

Figure 23. Double pendulum results for case (b).

5. Conclusions

A general regularized contact model was characterized and implemented. The model is suitable for real-time simulation, e.g. in robotic applications, since the resulting ordinary differential equations are simple, and can be solved using explicit solvers. The model is separated into compliant normal and tangential force models.

For the normal model, a novel method of computing the damping coefficient was introduced. The exact relationship between the coefficients of damping and restitution was derived. As a result, the model behavior is consistent with any prescribed value (or experimental function) for the coefficient of restitution. The normal force model can therefore be used to simulate elastic as well as nearly-plastic impacts, and is not restricted to a specific range of impact velocities. The vectorized tangential friction model correctly includes stick-slip behavior and the dwell-time frictional lag effect. The model behavior was shown to be qualitatively consistent with experimental observations.

Numerical simulation examples of a sphere colliding on a plane and on the interior surface of a cylinder under the action of gravity were provided. The resulting dynamic behavior is physically realistic and satisfies the condition $|\mathbf{v}| = R|\boldsymbol{\omega}|$ once the state of pure rolling is reached. The model was also used to simulate the collision of the tip of a double pendulum on a plane. The double pendulum simulation results were compared to a benchmark simulation and found to be in good agreement.

The authors are currently developing experiments in an effort to validate the contact model proposed here, and to determine empirical values of the parameters appearing in our model.

Acknowledgement

Funding of this research is provided by the Natural Sciences and Engineering Research Council of Canada.

References

1. Ahmed, S., Lankarani, H.M. and Pereira, M.F.O.S., 'Frictional impact analysis in open-loop multibody mechanical systems', *Transactions of the ASME Journal of Mechanical Design* **121**, 1999, 119–127.
2. Armstrong, B., *Control Machine Friction*, Kluwer Academic Publishers, Dordrecht, 1991.
3. Battle, J.A., 'On Newton's and Poisson's rules of percussive dynamics', *Transactions of the ASME Journal of Applied Mechanics* **60**, 1993, 376–381.
4. Bell, R. and Burdekin, M., 'An investigation into the mechanism of frictional damping of machine tools slideways', *Proceedings of the Institute of Mechanical Engineers, Applied Mechanics Group* **184**(59), 1969, 1088–1096.
5. Brogliato, B., *Nonsmooth Impact Mechanics*, Springer, London, 1996.
6. Canudas de Wit, C., Olson, H., Astrom, K.J. and Lischinsky, P., 'A new model for control of systems with friction', *IEEE Transaction on Automatic Control* **40**(3), 1995, 419–425.
7. de Carufel, J., Martin, E. and Piedbœuf, J.-C., 'Control strategies for hardware-in-the-loop simulation of flexible space robots', *IEEE Proceedings-D: Control Theory and Applications* **147**(6), 2000, 569–579.
8. Glocker, C. and Pfeiffer, F., 'Dynamical systems with unilateral contacts', *Nonlinear Dynamics* **3**, 1992, 107–115.
9. Goldsmith, W., *Impact: The Theory and Physical Behavior of Colliding Solids*, Edward Arnold, London, 1960.
10. Han, I. and Gilmore, B.J., 'Multi-body impact motion with friction – Analysis, simulation, and experimental validation', *ASME Journal of Mechanical Design* **115**, 1993, 412–422.
11. Hunt, K.H. and Crossley, F.R.E., 'Coefficient of restitution interpreted as damping in vibroimpact', *Transactions of the ASME Journal of Applied Mechanics, Series E* **42**, 1975, 440–445.
12. Jimenez, P., Thomas, F. and Torras, C., '3D collision detection: A survey', *Computers & Graphics* **25**(2), 2001, 269–285.
13. Johnson, K.L., *Contact Mechanics*, Cambridge University Press, London, 1985.
14. Keller, J.B., 'Impact with friction', *ASME Journal of Applied Mechanic* **53**, 1986, 1–4.
15. Khulief, Y.A. and Shabana, A.A., 'A continuous force model for the impact analysis of flexible multibody systems', *Mechanism and Machine Theory* **22**(3), 1987, 213–224.
16. Lankarani, H., 'Contact/impact dynamics applied to crash analysis', in *Proceedings of the NATO-ASI on Crashworthiness of Transportation Systems: Structural Impact and Occupant Protection*, Vol. 1, Tróia, Portugal, 1996, 255–283.
17. Lankarani, H.M. and Nikravesh, P.E., 'Application of the canonical equations of motion in problems of constrained multibody systems with intermittent motion', in *ASME Design Automation Conference*, Orland, FL, ASME, New York, ASME-Paper No. 88-DAC-51, 1988.

18. Lankarani, H.M. and Nikravesh, P.E., 'A contact force model with hysteresis damping for impact analysis of multibody systems', *ASME Journal of Mechanical Design* **112**, 1990, 369–376.
19. L'Archevêque, R., Doyon, M., Piedbœuf, J.-C. and Gonthier, Y., 'SYMOFROS: Software architecture and real time issues', in *DASIA 2000 – Data Systems in Aerospace*, Montreal, Canada, ESA, SP-457, 2000, 41–46.
20. Lichtenberg, A. and Liebermann, M., 1992, *Regular and Chaotic Dynamics*, Springer-Verlag, New York.
21. Lin, M. and Gottschalk, S., 'Collision detection between geometric models: A survey', in *The Proceedings of IMA Conference on Mathematics of Surfaces*, R. Cripps (ed.), University of Birmingham, 1998, 37–56.
22. Lüder, J., *Ein Beitrag zur Modellbildung von reibungsbehafteten Kontakten mit wechselnden Strukturen in Mehrkörpersystemen*, Berichte aus dem Maschinenbau, Shaker Verlag, Aachen, 2000.
23. Ma, O., 'CDT – A general contact dynamics toolkit', in *Proceedings of the 31st International Symposium on Robotics*, 2000, 468–473.
24. Marhefka, D.W. and Orin, D.E., 'A compliant contact model with nonlinear damping for simulation of robotic systems', *IEEE Transactions on Systems, Man and Cybernetics – Part A: Systems and Humans* **29**(6), 1999, 566–572.
25. Piedbœuf, J.-C., de Carufel, J., Aghili, F. and Dupuis, E., 'Task Verification Facility for the Canadian Special Purpose Dextrous Manipulator', in *1999 IEEE International Conference on Robotics and Automation*, Detroit, MI, 1999, 1077–1083.
26. Rabinowicz, E., 'Stick and slip', *Scientific American* **194**(5), 1956, 109–118.
27. Shi, P. and McPhee, J., 'Dynamics of flexible multibody systems using virtual work and linear graph theory', *Multibody System Dynamics* **4**, 2000, 355–381.
28. Stoianovici, D. and Hurmuzlu, Y., 'A critical study of the applicability of rigid-body collision theory', *ASME Journal of Applied Mechanics* **63**, 1996, 307–316.
29. Stronge, W.J., *Impact Mechanics*, Cambridge University Press, Cambridge, 2000.
30. Tenaglia, C.A., Orin, D.E., LaFarge, R.A. and Lewis, C., 'Toward development of generalized contact algorithm for polyhedral objects', in *Proceedings of the 1999 IEEE International Conference on Robotics and Automation*, 1999, 2887–2892.
31. Vielsack, P., 'Regularisierung des Haftzustandes bei Coulombscher Reibung', *Zeitschrift für angewandte Mathematik und Mechanik* **8**(76), 1996, 439–446.
32. Wang, Y. and Mason, M.T., 'Two-dimensional rigid-body collisions with friction', *ASME Journal of Applied Mechanics* **59**(3), 1992, 635–642.
33. Wehage, R.A., 'Generalized coordinate partitioning in dynamic analysis of mechanical systems', Ph.D. Thesis, University of Iowa, 1980.
34. Whittaker, E.T., *Analytical Dynamics*, 4th edition, Cambridge University Press, London, 1937.
35. Wittenburg, J., *Dynamics of Systems of Rigid Bodies*, B.G. Teubner, Stuttgart, 1977.